



Effects of Constituent Materials on Heat Generation in Individual EDLC Electrodes

Obaidallah Munteshari,^{1,2} Jonathan Lau,^{3,*} David S. Ashby,^{3,*} Bruce Dunn,^{3,**} and Laurent Pilon^{1,**,z}

¹Mechanical and Aerospace Engineering Department, Henry Samueli School of Engineering and Applied Science, University of California, Los Angeles, California 90095, USA

²Mechanical Engineering Department, King Fahd University of Petroleum and Minerals (KFUPM), Dhahran 31261, Saudi Arabia

³Materials Science and Engineering Department, Henry Samueli School of Engineering and Applied Science, University of California, Los Angeles, California 90095, USA

This study aims to investigate the effect of electrode composition on heat generation in electric double layer capacitor (EDLC) electrodes under galvanostatic cycling. EDLCs consist of two identical electrodes usually made of a mixture of (i) carbon-based material, (ii) binder, and (iii) other conductive additives. These constituents were found to influence the capacitance and internal resistance of the device and the heat generation rate in the positive and negative electrodes. Indeed, the heat generation rate was measured using an isothermal calorimeter in both electrodes of five EDLC devices with different electrode compositions but the same electrolyte consisting of 1 M LiPF₆ in EC:DMC. The reversible heat generation rates at the positive and negative electrodes were nearly identical in absence of CMC. However, in devices containing CMC, the reversible heat generation rate in the positive electrode was significantly larger than that in the negative electrode. Such asymmetric heating was attributed to asymmetry in the charging mechanism due to the overscreening effect caused by interactions between the anionic functional groups of CMC and the cations at the negative electrode.

© The Author(s) 2018. Published by ECS. This is an open access article distributed under the terms of the Creative Commons Attribution Non-Commercial No Derivatives 4.0 License (CC BY-NC-ND, <http://creativecommons.org/licenses/by-nc-nd/4.0/>), which permits non-commercial reuse, distribution, and reproduction in any medium, provided the original work is not changed in any way and is properly cited. For permission for commercial reuse, please email: oa@electrochem.org. [DOI: 10.1149/2.0771807jes]



Manuscript submitted February 19, 2018; revised manuscript received April 27, 2018. Published May 22, 2018.

Electric double layer capacitors (EDLCs) have received significant attention in recent years for electrical energy storage applications in particular those requiring rapid charging/discharging, such as regenerative braking in electric vehicles,¹ smart grids,² and renewable energy harvesting systems.³⁻⁵ Indeed, EDLCs can provide higher power density, higher cycle efficiency, and longer lifetime than batteries.^{4,6} EDLC devices consist typically of two carbon-based electrodes partitioned by a separator immersed in aqueous or organic electrolytes. EDLCs store electrical energy in the electrical double layer of ions forming at electrode/electrolyte interface.

Heat generation in EDLC is a major concern since these devices are usually cycled under high current density resulting in excessive temperature rise.⁷ This, in turn, can lead to (i) accelerated cell aging,⁸⁻¹⁰ (ii) increased self-discharge rates,^{9,11} and possibly (iii) electrolyte decomposition and evaporation.^{9,12} Heat generation in EDLCs can be classified into irreversible and reversible heat generation rates.^{7,13-17} Irreversible heat generation has been attributed, both theoretically and experimentally, to Joule heating.^{7,9,11,13-20} It is constant throughout the EDLC cell and equal to the product of the EDLC internal resistance and the square of the imposed current.^{7,14-16} On the other hand, reversible heat generation rate in the entire device was theoretically and experimentally found to be exothermic during charging and endothermic during discharging.^{7,14-16} The time-averaged reversible heat generation over a charging step was shown to be proportional to the imposed current under galvanostatic cycling.^{7,14-16} Experimentally, reversible heat generation has been assumed to be identical in both the positive and negative electrodes.¹⁴ However, our recent experimental study has demonstrated that reversible heat generation rate was systematically different in identical positive and negative carbon-based electrodes of EDLC cell with both organic and aqueous electrolytes.²¹ In fact, averaged over a constant current charging step, the reversible heat generation at the positive electrode was linearly proportional to the current while it was independent of current and nearly zero at the negative electrode.²¹ This thermal behavior could be attributed to (i)

parasitic reversible redox reactions involving the CMC binder,²²⁻²⁴ (ii) reversible ion solvation/desolvation,²⁵ (iii) differences in ion size and diffusion coefficient in the electrolytes,¹⁶ and/or (iv) differences in ion adsorption and desorption mechanisms at the electrode surface.²⁶

The present study aims to elucidate the physicochemical phenomena responsible for asymmetric heat generation in otherwise identical positive and negative electrodes of EDLC cells. To do so, the effect of each electrode constituent on the heat generation in the positive and negative electrodes of EDLC devices were systematically investigated experimentally using the previously developed isothermal calorimeter.²¹

Background

A few experimental and numerical studies have paid attention to reversible heat generation rate in EDLCs.^{7,13-17,21} Most experimental studies measured the total heat generation rate in commercial or laboratory scale EDLC devices and typically assumed that the heat generation rate was identical at both electrodes.^{7,13,14} However, we recently established experimentally that the reversible heat generation rates at positive and negative electrodes of EDLC cells could be different despite using identical activated carbon-based electrodes and different aqueous and organic electrolytes, as previously discussed.²¹

EDLC electrodes are usually made of a mixture of (i) 70 to 95 wt% carbon-based material, (ii) binder, and (iii) other conductive additives (e.g., carbon black) to enhance the electrochemical properties of the electrodes.²⁷⁻³⁵ Carbon-based materials, including activated carbons (ACs), carbon cloth, carbon aerogels, templated porous carbon (TC), activated carbon fiber (ACF), and carbon nanotube (CNT), are the most widely used materials for EDLCs since they are electrically conducting and chemically stable in various types of electrolyte under a wide range of potential windows and temperatures.^{36,37} Moreover, they are abundant, inexpensive, easily-processable, and environmentally friendly.^{38,39}

The main function of the binder is to hold the electrode constituents together and to improve adhesion to the current collectors.⁴⁰ Excessive amounts of binder could increase the electrical resistance of the electrode.³³ Polytetrafluoroethylene (PTFE)^{28,30,33,34} and

*Electrochemical Society Student Member.

**Electrochemical Society Member.

^zE-mail: pilon@seas.ucla.edu

polyvinylidene difluoride (PVdF)^{27,31,32} are the most widely used binders for EDLC electrodes. Some studies used derivatives of these two binders, such as polyvinylidene fluoride-hexafluoropropylene (PVdF-HFP)⁴¹ and Nafion.⁴² Recently, cellulose and its derivatives have also been employed in electrochemical energy storage devices as substrate, separator, and electrode binder for their low cost, environmental friendliness, and easy processability.^{40,43–55} For example, sodium carboxymethyl cellulose (CMC-Na) has attracted attention as an electrode binder for EDLCs.^{40,51,54} Carbon-based electrodes with CMC binder showed similar capacitance and cycling stability as electrodes using conventional binders (i.e., PVdF).⁴³ Also, CMC has been used as a binder for lithium-ion batteries.^{44–50,52,53} Replacing Na⁺ in CMC-Na by Li⁺ was found to improve the performance of lithium-ion batteries as CMC-Li enriched the electrolyte with Li⁺ ions.^{24,56} Note also that Na⁺ ions in the CMC-Na binder tend to dissociate in the electrolyte forming anionic functional groups.^{22–24} These functional groups could interact with the cations in the electrolyte influencing heat generation in each electrode.

The conventional view of EDLC suggests that the electrodes charge by counter-ion adsorption. However, recent studies have shown that the EDLC electrodes can be charged by different mechanisms including counter-ion adsorption, co-ion desorption, and/or ion exchange.²⁶ In addition, different mechanisms can take place in a given electrode at different potentials.⁵⁷ Forse et al.²⁶ introduced the so-called charging mechanism parameter to account for different charging mechanisms taking place in the positive and negative electrodes. New experimental techniques, including nuclear magnetic resonance spectroscopy,⁵⁸ X-ray transmission,⁵⁹ electrochemical quartz crystal microbalance,⁵⁷ and infrared spectroscopy,⁶⁰ as well as molecular dynamic simulations⁶¹ have established that the electrolyte, electrode constituent materials, and the polarization of the electrode could affect the charging mechanism of EDLC electrodes and thus the heat generation therein.

The present study aims to investigate the effect of binder and other electrode constituents on the charging mechanism and the associated irreversible and reversible heat generation rates in both positive and negative carbon-based electrodes. The current work complements our previous study which focused on heat generation in EDLC with different aqueous and organic electrolytes and electrodes made of activated carbon, CMC and styrene butadiene rubber (SBR) as thickening agent/binder, and TX100 surfactant.

Materials and Methods

EDLC devices.—Five EDLC devices were assembled to investigate the effect of each constituent material of the electrode on heat generation in both positive and negative electrodes. The two electrodes of each device were identical and made of four different constituents namely (i) activated carbon (YP50F, Kuraray Chemical) with surface area of 1600 m²/g,⁶² (ii) non-ionic surfactant (TX100, Sigma-Aldrich), and (iii) carboxymethyl cellulose (CMC) (DOW Chemical) and (iv) styrene butadiene rubber (SBR) (MTI Corporation) as binder/thickening agent. Table I summarizes the five electrode compositions considered in this study.

The electrodes were synthesized by mixing, in DI water, the different electrode constituents (Table I). The mixture was drop-cast

onto 1 × 1 cm² 316 stainless steel plates, serving as current collectors, previously treated by oxygen plasma to enhance their hydrophilicity and ensure even spreading of the slurry containing polar solvents.⁶³ The use of oxygen plasma has not been shown to introduce an interfacial resistance detrimental to electrochemical cycling, even for high-rate pseudocapacitors.⁶³ The mass loading, for each electrode, was 2.5 mg/cm² with a thickness of 50 ± 5 μm. The electrodes were dried under vacuum at 120°C for 24 hours before being placed in a glove box under argon atmosphere. The five EDLC devices tested consisted of two identical activated carbon electrodes supported by their 316 stainless steel current collector separated by a 350 μm glass fiber separator (GF85 filter, AdvantecMFS Inc.) immersed in 1 M of lithium hexafluorophosphate (LiPF₆, Oakwood Chemical) in ethylene carbonate:dimethyl carbonate (EC:DMC) (Sigma-Aldrich) with 1:1 volume ratio. LiPF₆ in EC:DMC was chosen for its superior stability compared to other electrolytes (e.g., citric acid and TBATFB in acetonitrile) used in our previous study.²¹ Finally, the EDLC devices were assembled, installed, and sealed in the electrochemical test section inside the glove box to avoid exposure to ambient atmosphere.

Isothermal calorimeter.—We recently reported on the design, fabrication, and demonstration of an isothermal calorimeter apparatus to measure the instantaneous heat generation rate in the individual electrodes of EDLC devices.²¹ Details of the experimental setup, validation, and data analysis have been reported and need not be repeated.²¹ In brief, the calorimeter used thermoelectric heat flux sensors in thermal contact with each electrode to measure the time-dependent heat generation rate therein with accuracy and uncertainty of ±10 μW and 3%, respectively.²¹

The instantaneous heat generation rate $\dot{Q}_i(t)$ (in mW) at electrode “*i*” can be expressed as,²¹

$$\dot{Q}_i(t) = \frac{\Delta V_i(t)}{S_i} A_i \quad \text{with } i = + \text{ or } - \quad [1]$$

where $\Delta V_i(t)$ is the voltage difference (in μV) measured in the heat flux sensor while S_i and A_i are the sensor temperature-dependent sensitivity (in μV/(mW/cm²)) and footprint area of the electrode (in cm²), respectively. The subscript “*i*” refers to either the positive “+” or negative “−” electrode. The total heat generation rate in the entire cell (denoted by subscript “*T*”) can be expressed as $\dot{Q}_T(t) = \dot{Q}_+(t) + \dot{Q}_-(t)$.

The instantaneous heat generation rate $\dot{Q}_i(t)$ is the superposition of the irreversible $\dot{Q}_{irr,i}(t)$ and reversible $\dot{Q}_{rev,i}(t)$ heat generation rates, i.e., $\dot{Q}_i(t) = \dot{Q}_{irr,i}(t) + \dot{Q}_{rev,i}(t)$. We prove later in the manuscript that the irreversible heat generation rate $\dot{Q}_{irr,i}(t)$ was due to Joule heating which, under constant current cycling, remains unchanged during charging and discharging. Then, the instantaneous $\dot{Q}_{irr,i}(t)$ (in mW) could be approximated as the time-averaged irreversible heat generation rate $\bar{Q}_{irr,i}$ (in mW). Moreover, by definition, time-averaging the reversible heat generation rate $\dot{Q}_{rev,i}(t)$ at electrode “*i*” over an entire cycle yields $\bar{Q}_{rev,i} = 0$. Thus, the irreversible heat generation rate $\bar{Q}_{irr,i}$ at electrode “*i*” subjected to a galvanostatic cycle of period t_{cd} (in s) can be expressed as,

$$\bar{Q}_{irr,i} = \frac{1}{t_{cd}} \int_{(n-1)t_{cd}}^{nt_{cd}} \dot{Q}_i(t) dt \quad \text{with } i = + \text{ or } - \quad [2]$$

where n is the cycle number, taken sufficiently large to have reached oscillatory steady state. In addition, the instantaneous reversible heat generation rate $\dot{Q}_{rev,i}(t)$ (in mW) at each electrode or in the device can be evaluated by subtracting the irreversible heat generation rate $\bar{Q}_{irr,i}$ (Equation 2) from the instantaneous heat generation rate $\dot{Q}_i(t)$, i.e.,

$$\dot{Q}_{rev,i}(t) = \dot{Q}_i(t) - \bar{Q}_{irr,i} \quad \text{with } i = T, +, \text{ or } - \quad [3]$$

Finally, in order to effectively compare the reversible heat generation rate at each electrode, the instantaneous reversible heat generation rate

Table I. Electrodes compositions for the five carbon-based EDLC devices studied.

Device No.	AC (wt%)	SBR (wt%)	TX100 (wt%)	CMC (wt%)	Comments
1	80	13.5	5	1.5	Reference ²¹
2	93.5	0	5	1.5	w/o SBR
3	86	12	0	2	w/o TX100
4	83	12	5	0	w/o CMC
5	79.5	11.6	4.3	4.6	3×CMC

$\dot{Q}_{rev,i}(t)$ was averaged over a galvanostatic charging step of duration t_c to yield the time-averaged reversible heat generation rate during charging $\bar{Q}_{rev,i}^c$ (in mW),

$$\bar{Q}_{rev,i}^c = \frac{1}{t_c} \int_{(n-1)t_{cd}}^{(n-1)t_{cd}+t_c} \dot{Q}_{rev,i}(t) dt \quad \text{with } i = T, +, \text{ or } -. \quad [4]$$

Experimental procedure.—Cyclic voltammetry (CV) was used to determine the capacitance of the five EDLC devices featuring five different electrode compositions (Table I). The devices were cycled between 0 and 1 V for scan rates 1, 5, 10, 15, and 20 mV/s. The cell's integral gravimetric capacitance C_g (in F/g) was evaluated by integrating the area enclosed by the CV curve plotting measured current (in mA) versus imposed potential ψ_s (in V) for a given scan rate ν (in mV/s) and potential window between ψ_{min} and ψ_{max} as,⁶⁴

$$C_g(\nu) = \frac{1}{m(\psi_{max} - \psi_{min})} \oint \frac{I}{2\nu} d\psi \quad [5]$$

where m is the mass of active materials loaded into both electrodes (in g).

The heat generation measurements at low current (i.e., $I \leq 1$ mA) fell below the detection level (< 0.01 mW) of the calorimeter introducing a significant error in the measurements. Thus, the heat generation rates were measured under galvanostatic cycling for imposed constant current $I = 2, 3, 4, 5,$ and 6 mA to obtain $\dot{Q}_i(t)$, $\bar{Q}_{irr,i}$, $\dot{Q}_{rev,i}(t)$, and $\bar{Q}_{rev,i}^c$.

The internal resistance R_s (or DC resistance) (in Ω) was determined from the IR drop at charging/discharging transitions of potential curve under galvanostatic cycling according to,⁶⁵⁻⁶⁸

$$R_s(I) = \frac{\psi_s(t_c^+) - \psi_s(t_c^-)}{2I} \quad [6]$$

where $\psi_s(t_c^+)$ and $\psi_s(t_c^-)$ are the potentials across the EDLC cell at the end of the charging step and immediately after the beginning of the discharging step, respectively. Here, the IR drop ($\psi_s(t_c^+) - \psi_s(t_c^-)$) was obtained by estimating the cell potential $\psi_s(t_c^-)$ 10 ms after the beginning of the discharging step (i.e., $t_c^- - t_c^+ = 10$ ms) as suggested by Zhao et al.⁶⁶

Results and Discussion

Cyclic voltammetry curves and capacitance.—Figure 1 plots the measured CV curves of Devices 1 to 5 for scan rates (a) $\nu = 1$ mV/s and (b) $\nu = 20$ mV/s. In all cases, the mass loading was 5 mg/cm^2 for the entire cell and the potential window ($\psi_{max} - \psi_{min}$) was fixed to 1 V for all devices considered to facilitate comparison. The CV curves of all devices featured rectangular and symmetrical shapes indicating near ideal capacitive behavior for scan rate $\nu = 1$ mV/s. However, at high scan rate (Figure 1b), the CV curves of Device 4 featured significant deviation from this ideal behavior due to apparent resistive losses in the absence of CMC binder.

Moreover, Figure 2 shows the gravimetric capacitance $C_g(\nu)$ of the five EDLC devices as a function of scan rate ν ranging from 1 to 20 mV/s. It indicates that the capacitance $C_g(\nu)$ of all devices decreased with increasing scan rate. However, the capacitance of Device 4 (w/o CMC) decreased faster than that of Devices 1, 2, 3, and 5. In addition, it is interesting to note that Devices 2, 3, 4, and 5 featured lower capacitance than Device 1. Thus, each constituent material of the reference electrode was essential to enhancing electrode performance. The absence of SBR (Device 2) and TX100 (Device 3) had nearly the same effect in reducing the cell capacitance. On the other hand, the absence of CMC binder (Device 4) had a significant negative effect on the device capacitance. Hence, CMC binder was essential to the electrode electrical conductivity by binding activated carbon particles to each other and to the current collector. However, it is interesting to note that increasing the amount of CMC binder (Device 5) led to a

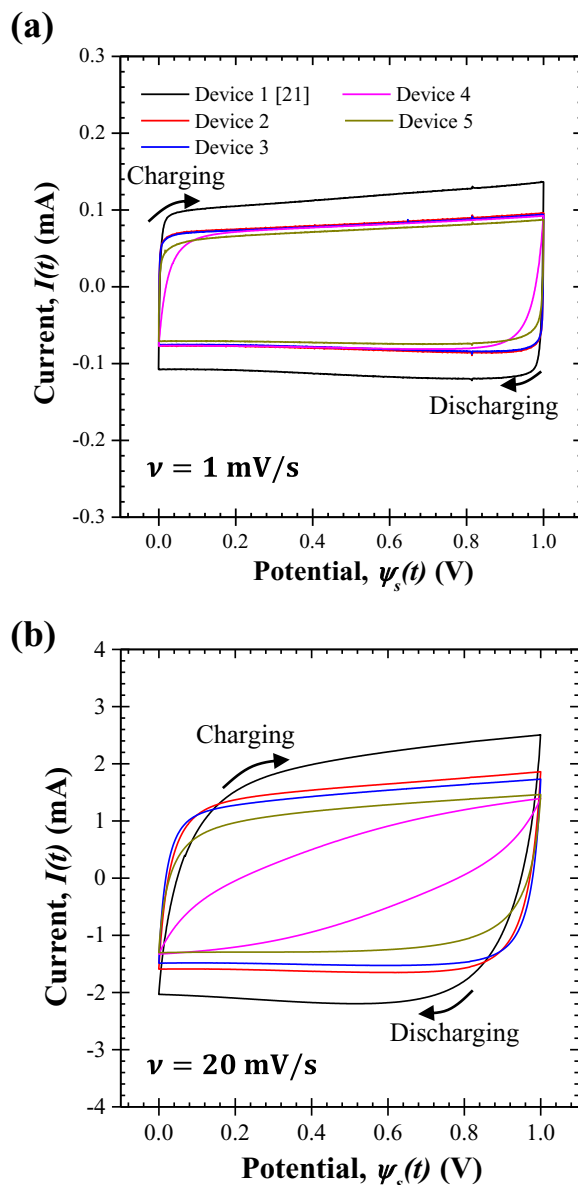


Figure 1. CV curves for Devices 1,²¹ 2, 3, 4, and 5 (see Table I) for scan rates (a) $\nu = 1$ mV/s and (b) $\nu = 20$ mV/s and potential window ($\psi_{max} - \psi_{min}$) = 1 V.

decrease in capacitance. This can be attributed to the fact that excessive amount of binder decreased the accessible electrochemically active surface area of the electrodes.³³

Internal resistance R_s .—Figure 3 shows the potential $\psi_s(t)$ across the cell as a function of time t during galvanostatic cycling for Devices 1 to 5 for constant current (a) $I = 2$ mA and (b) $I = 6$ mA and potential window of 1 V. Figure 3 indicates that, for all five devices, the potential varied linearly with time between the minimum potential ψ_{min} and maximum potential ψ_{max} , except for the IR drop $\psi_s(t_c^+) - \psi_s(t_c^-)$ occurring at the transition after charging and discharging steps. The latter was more significant in the absence of CMC binder (Device 4). In fact, for $I = 6$ mA, the IR drop in Device 4 was nearly equivalent to the potential window considered, i.e., $[\psi_s(t_c^+) - \psi_s(t_c^-)] \simeq (\psi_{max} - \psi_{min})$. Thus, the heat generation measurements for Device 4 were only reported for current I ranging from 2 to 4 mA.

Figure 4 shows (a) the internal resistance $R_s(I)$ estimated from Equation 6 and (b) the period of the galvanostatic cycle t_{cd} as functions

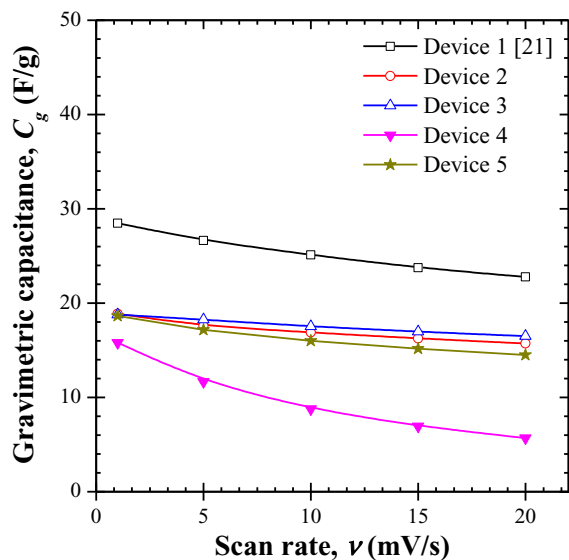


Figure 2. Integral gravimetric capacitance $C_g(\nu)$ of Devices 1,²¹ 2, 3, 4, and 5 (Table I) as a function of scan rate ν for potential window of 1 V.

of imposed current I for Devices 1 to 5. For all devices, the internal resistance was almost independent of current I except for Device 4 when R_s decreased with increasing current I . Interestingly, the absence of SBR and TX100 reduced the resistance of Devices 2 and 3 compared with Device 1. However, their absence also reduced the cell capacitance C_g (Figure 2). Note also that Device 4 featured the largest resistance of all devices due to the absence of CMC binder, confirming previous observations on CV curves (Figure 1). Finally, increasing the amount of CMC by three times (Device 5) did not affect the resistance of the device, however, it reduced its capacitance (Figure 2), as previously discussed.

Instantaneous and irreversible heat generation rates.—Figure 5 shows the temporal evolution of the measured heat generation rates $\dot{Q}_+(t)$ at the positive electrode, $\dot{Q}_-(t)$ at the negative electrode, and $\dot{Q}_T(t) = \dot{Q}_+(t) + \dot{Q}_-(t)$ in the entire cell as functions of dimensionless time t/t_{cd} for five consecutive galvanostatic cycles under constant current $I = 4$ mA for (a) Device 1, (b) Device 2, (c) Device 3, (d) Device 4, and (e) Device 5. It is interesting to note that measurements of the instantaneous heat generation rates were repeatable for all devices assembled. However, the respective magnitude and shape differed significantly for a given device and among the five devices considered. The heat generation rate in Devices 1 and 5 was slightly larger than that in Devices 2 and 3 due to their larger internal resistance R_s (Figure 4a). In Devices 1, 2, 3 and 5, the heat generation rate in the negative electrode was systematically smaller than that in the positive electrode. By contrast, the heat generation rates $\dot{Q}_+(t)$ and $\dot{Q}_-(t)$ were nearly identical in Device 4 (w/o CMC).

Finally, Figure 5f shows the total irreversible heat generation rate $\bar{Q}_{irr,T}$ plotted against the predicted Joule heating \bar{Q}_J (in mW) given by $\bar{Q}_J = R_s(I)^2$ in the entire cell under galvanostatic cycling with current I ranging between 2 and 6 mA for Devices 1 to 5. Here, $R_s(I)$ was the internal resistance measured as a function of current I (Figure 4a). Figure 5f indicates that the total irreversible heat generation rate $\bar{Q}_{irr,T}$ in all devices was in excellent agreement with predictions for the heat generation rate \bar{Q}_J due to Joule heating. In other words, Joule heating was the dominant source of irreversible heat generation in the five EDLC devices considered (Table I). In addition, Device 4 featured much larger $\bar{Q}_{irr,T}$ than that of Devices 1, 2, 3, and 5 due to its larger internal resistance $R_s(I)$ caused by the absence of CMC binder (Figure 4a), as previously discussed.

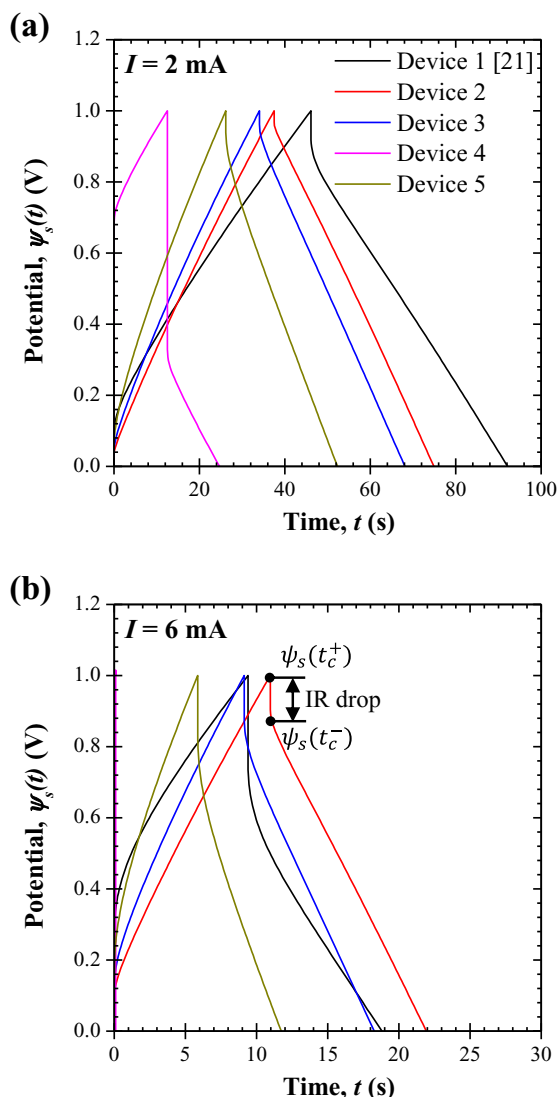


Figure 3. Galvanostatic charging-discharging curves of Devices 1,²¹ 2, 3, 4, and 5 (Table I) for current (a) $I = 2$ mA and (b) $I = 6$ mA with potential window limited to 1 V.

Reversible heat generation rates.—Figure 6 shows the instantaneous reversible heat generation rates (a) $\dot{Q}_{rev,T}(t)$ in the entire cell, (b) $\dot{Q}_{rev,+}(t)$ at the positive electrode, and (c) $\dot{Q}_{rev,-}(t)$ at the negative electrode as functions of dimensionless time t/t_{cd} for current $I = 4$ mA for Devices 1 to 5. Two cycles were plotted for each device, namely cycle 10 (solid line) and cycle 15 (dashed line). First, Figures 6a, 6b, and 6c indicate that $\dot{Q}_{rev,T}(t)$, $\dot{Q}_{rev,+}(t)$, and $\dot{Q}_{rev,-}(t)$ were reproducible from cycle to cycle. In addition, Figure 6a establishes that the total reversible heat generation rate $\dot{Q}_{rev,T}(t)$ for the entire cell was exothermic for most of the charging step and endothermic during most of the discharging step. This finding was consistent with previous measurements and numerical predictions of reversible heat generation in EDLC devices.^{7,13–16} The reversible heat generation rate $\dot{Q}_{rev,+}(t)$ at the positive electrode (Figure 6b) was also exothermic during charging and endothermic during discharging for all five devices considered. However, $\dot{Q}_{rev,-}(t)$ at the negative electrode for Devices 1, 2, 3, and 5 was exothermic and endothermic during both charging and discharging steps. The same observations were reported previously with electrodes similar to those of Device 1 but with different electrolytes.²¹ In this context, it is interesting to note that Device 4 featured reversible heat generation rate $\dot{Q}_{rev,-}(t)$ at the negative electrode nearly identical to $\dot{Q}_{rev,+}(t)$ at the positive electrode, i.e.,

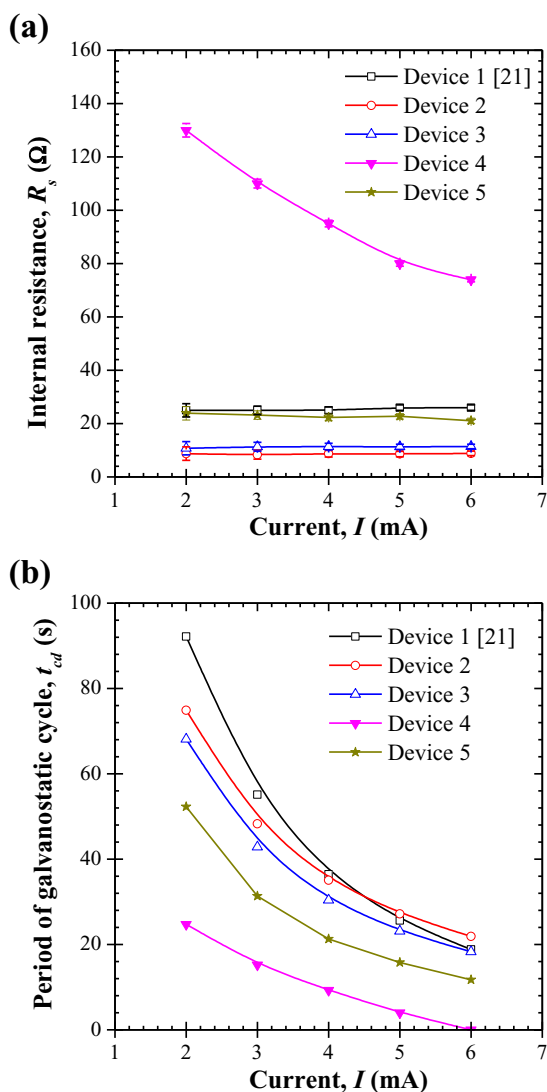


Figure 4. (a) Internal resistance R_s and (b) period of galvanostatic cycle t_{cd} as functions of current I for Devices 1,²¹ 2, 3, 4, and 5 (Table I) with current I ranging from 2 to 6 mA and potential window of 1 V.

$\dot{Q}_{rev,+}(t)$ and $\dot{Q}_{rev,-}(t)$ were exothermic during the entire charging step and endothermic during the entire discharging step.

Figure 6 also shows the time-averaged reversible heat generation rates during the charging step (d) $\bar{Q}_{rev,T}^c$ in the entire cell, (e) $\bar{Q}_{rev,+}^c$ at the positive electrode, and (f) $\bar{Q}_{rev,-}^c$ at the negative electrode as functions of current I ranging between 2 and 6 mA for the five EDLC devices considered (Table I). Here, the reported values of $\bar{Q}_{rev,i}^c$ were averaged over 10 cycles and the error bars correspond to two standard deviations or 95% confidence interval. The linear fit, obtained by least square method, is also shown to guide the eye. Interestingly, the time-averaged reversible heat generation rates $\bar{Q}_{rev,T}^c$ in the entire cell (Figure 6d) and $\bar{Q}_{rev,+}^c$ at the positive electrode (Figure 6e) were proportional to the current I for all devices, as previously observed experimentally^{14,21} and predicted numerically.¹⁵ By contrast, $\bar{Q}_{rev,-}^c$ at the negative electrode (Figure 6f) was nearly constant and close to zero for Devices 1, 2, and 5 and negative for Device 3. However, Figures 6e and 6f indicate that, in Device 4 (no CMC), $\bar{Q}_{rev,-}^c$ at the negative electrode was nearly identical to $\bar{Q}_{rev,+}^c$ at the positive electrode. In summary, the reversible heat generation rates at the positive and negative electrodes were asymmetric in devices with

electrodes containing CMC (Devices, 1, 2, 3, and 5) but were nearly identical in electrodes without CMC (Device 4). Also, Device 3 (w/o TX100) featured more endothermic heating during charging step. In order to explain these observations, four hypotheses were examined including (i) parasitic reversible redox reactions involving the CMC binder,²²⁻²⁴ (ii) reversible ion solvation/desolvation,²⁵ (iii) differences in ion size and diffusion coefficient in the electrolytes,¹⁶ and (iv) asymmetric charging mechanisms.²⁶ Note that the present calorimeter was configured for two electrode configuration and could not provide the potential evolution across each electrode separately. However, Ania et al.⁶⁹ showed that, at low cell potential (i.e., $\psi_s \leq 1$ V), the potential difference was identical across the positive and negative electrodes of a symmetric EDLC cell in organic electrolyte.

(i) *Reversible redox reactions involving CMC binder.*—The above observations for Devices 1, 2, 3, and 5 could potentially be attributed to redox reaction involving the CMC binder. However in Device 5, the amount of CMC was increased by three orders of magnitude while the instantaneous reversible heat generation rate $\dot{Q}_{rev,-}(t)$ was nearly the same as that in the reference Device 1.

Furthermore, three-electrode measurements were performed on stainless steel current collectors (i) bare and (ii) coated with a layer of CMC. Figure 7 shows cyclic voltammetry of 1×1 cm² bare and CMC-coated stainless steel current collectors cycled in 1 M LiPF₆ EC:DMC with lithium metal counter and reference electrodes for scan rates $\nu = 10$ and 20 mV/s. The redox couple observed in the potential range from 2 to 4 V vs. Li (equivalent to -2 to 2 V operating window of a symmetric activated carbon EDLC) can be attributed to surface redox reactions on the stainless steel current collector. However, the current associated with these redox peak was less than 20 μ A, corresponding to a negligible contribution to heat generation. On the other hand, the CV curves of CMC-coated current collector did not feature any additional redox peak. In fact, the current decreased due to a reduction in the stainless steel surface area exposed. These results establish that redox reactions involving the CMC binder were not responsible for the endothermic heating observed at the negative electrode at the beginning of the charging step (Figure 6c).

(ii) *Ion solvation/desolvation.*—The size of Li⁺ ions is much smaller than that of PF₆⁻ and the solvation energies of Li⁺ and PF₆⁻ are -212.6 and -93.3 kcal/mol, respectively.²⁵ Hence, we speculated that the endothermic kink observed at the negative electrode at the beginning of the charging step was due to cations desolvation as they adsorbed into the carbon electrode pores and whose size distribution was affected by the presence of the CMC binder. In absence of CMC binder (Device 4), the electrode pore size distribution could be much larger than the ionic size of solvated Li⁺ (~ 0.41 nm⁷⁰) so that solvation/desolvation did not take place in the pores. In order to examine this hypothesis, pore size distribution of powder samples scraped from the electrode materials of Devices 1, 4, and 5 were measured by nitrogen adsorption method. The measurements were conducted using a Micromeritics ASAP 2010 system with ultra high purity nitrogen at 77 K. Powder samples were outgassed at 250°C overnight before testing. The pore size distribution curves were calculated from the nitrogen adsorption isotherms using the carbon slit pore geometry non-linear density function (NLDFT) model through the Micromeritics Microactive software.

Figure 8a shows the adsorption isotherms obtained for electrode materials of Devices 1, 4, and 5. The shape of the isotherm was characteristic of a Type I isotherm, indicating that the structure was composed primarily of micropores (< 2 nm).⁷¹ At high relative pressures, the lack of a gas uptake and appreciable hysteresis indicated that there were no mesopores (2–50 nm) or macropores (> 50 nm) in the structure. The small hysteresis between adsorption and desorption isotherms most likely originated from activated carbon particles and has commonly been observed in experimental adsorption curves for carbon powders.^{72,73} Figure 8b presents the derivative of pore volume with respect to pore width. The pore volume was normalized arbitrarily to better compare the different pore size distributions.

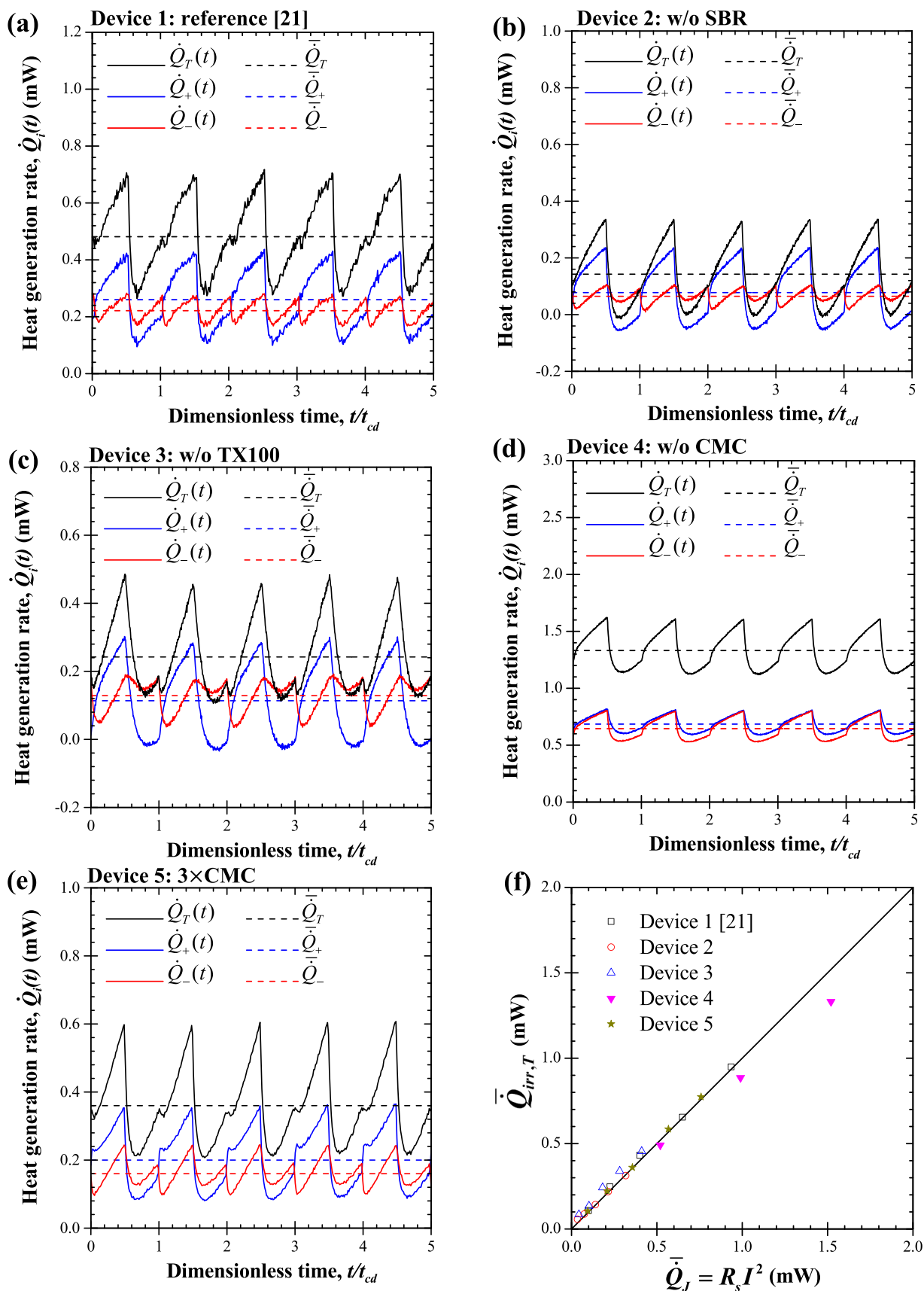


Figure 5. Five representative and consecutive charging-discharging cycles of heat generation rates $\dot{Q}_+(t)$ at the positive electrode, $\dot{Q}_-(t)$ at the negative electrode, and $\dot{Q}_T(t)$ in the entire cell as functions of the dimensionless time t/t_{cd} for current $I = 4$ mA in (a) Device 1,²¹ (b) Device 2, (c) Device 3, (d) Device 4, and (e) Device 5. (f) Irreversible heat generation rate $\bar{\dot{Q}}_{irr,T}$ under galvanostatic cycling versus predicted Joule heating $\bar{\dot{Q}}_J = R_s(I)I^2$ for current I ranging between 2 and 6 mA for Devices 1 to 5 using $R_s(I)$ shown in Figure 4a.

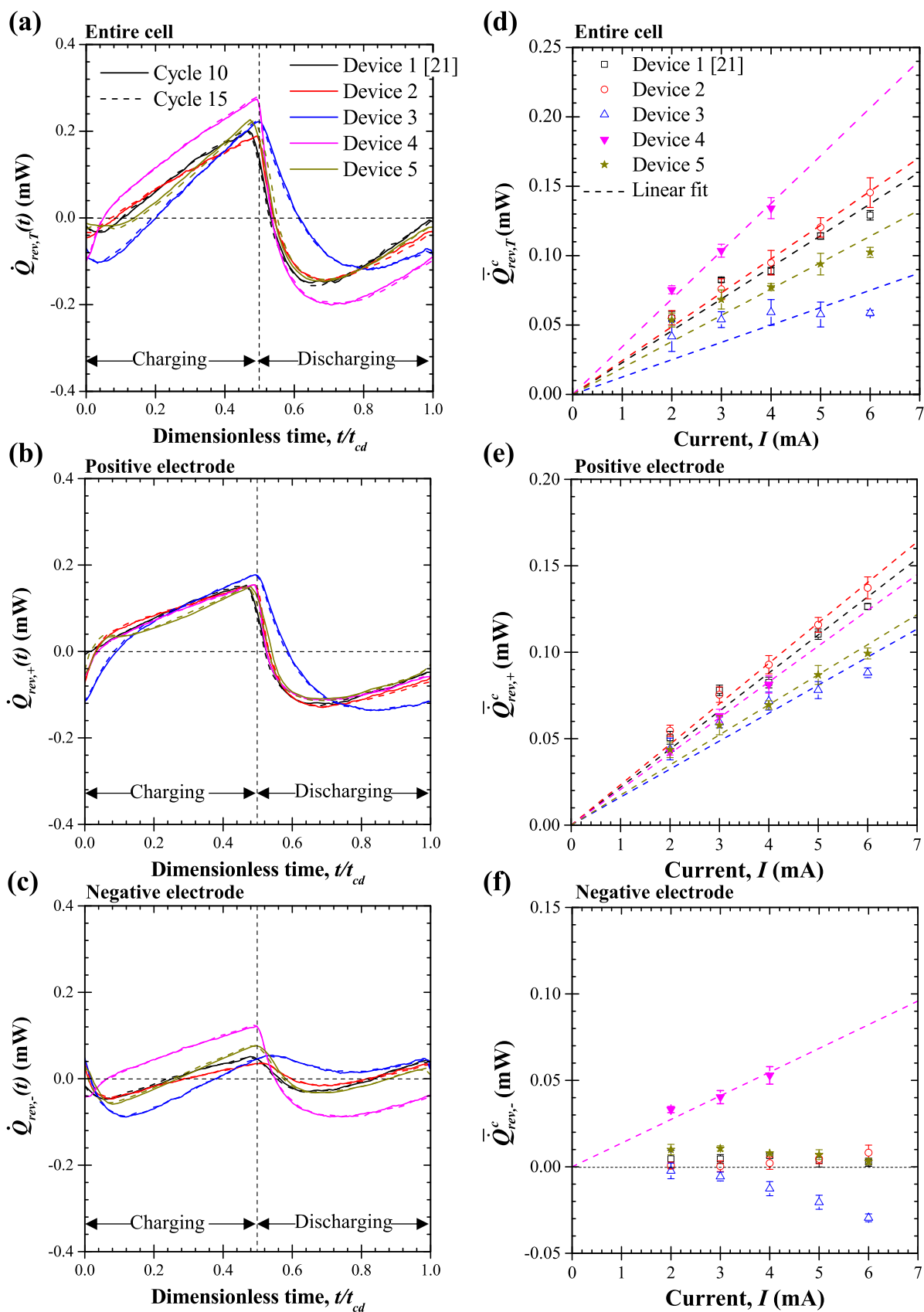


Figure 6. One charging-discharging cycle of the reversible heat generation rates (a) $\dot{Q}_{rev,T}$ in the entire cell, (b) $\dot{Q}_{rev,+}$ at the positive electrode, and (c) $\dot{Q}_{rev,-}$ at the negative electrode as functions of the dimensionless time t/t_{cd} for current $I = 4$ mA for Devices 1,²¹ 2, 3, 4, and 5. Time-averaged reversible heat generation rates during the charging step (d) $\bar{Q}_{rev,T}^c$ in the entire cell, (e) $\bar{Q}_{rev,+}^c$ at the positive electrode, and (f) $\bar{Q}_{rev,-}^c$ at the negative electrode as functions of current I ranging between 2 and 6 mA for Devices 1,²¹ 2, 3, 4, and 5.

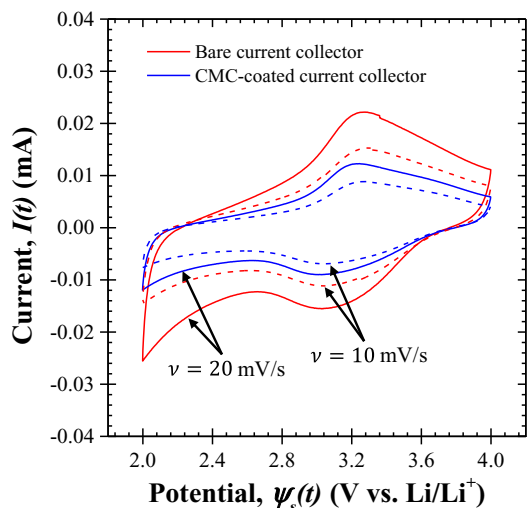


Figure 7. Cyclic voltammetry of 1×1 cm bare and CMC-coated stainless steel current collectors cycled in 1 M LiPF₆ EC:DMC with lithium metal counter and reference electrodes for potential window of 2 to 4 V vs. Li and scan rate $\nu = 10$ and 20 mV/s.

The difference in peak areas was associated with errors in the measured powder weight and distribution of electrode constituents. The bimodal pore size distribution, with the majority found between 0.8 and 1.2 nm, agreed well with pore size distribution reported in the literature for YP50F.⁷⁴ Similar pore widths for all three device compositions indicates that the presence of CMC did not have an appreciable effect on the pore size distribution and did not inhibit ions access to the pores of the YP50F particles. These observations establish that ion solvation/desolvation was not affected by the presence of CMC and thus was not responsible for the thermal behavior observed at the negative electrode.

(iii) *Differences in ion size and diffusion coefficient.*—Ion size and diffusion coefficient have been shown to affect only the magnitude of heat generation at the electrode but not the exothermic to endothermic nature of the heat generation processes.¹⁶ For example, the electrode with smaller counter-ion diameter featured larger reversible heat generation rate under galvanostatic cycling than the counter electrode.¹⁶ In addition, the reversible heat generation rate was found to be independent of diffusion coefficient of ions.¹⁶ However, the ion size could affect other phenomena taking place at the electrodes including charging mechanism.²⁶

(iv) *Charging mechanism.*—As ions adsorb on the electrode surface to form an EDL or disperse into the electrolyte, they release heat (exothermic) or absorb heat (endothermic), respectively.^{7,13–16,75} Thus, the reversible heat generation rate associated with changes in entropy of ions (entropy of mixing) depends strongly on the charging mechanism. Asymmetric heat generation in the devices containing CMC suggests that the charging mechanism at the positive and negative electrodes was also asymmetric. Indeed, CMC binder is a weak polyacid that interacts with cations in the electrolytes.^{22–24} In fact, Na⁺ in carboxymethyl (–CH₂COONa) groups and H⁺ in hydroxyl (–OH) groups of CMC binder have a tendency to dissociate in the electrolyte forming anionic functional groups (–CH₂COO[–]) and (–O[–]), respectively.^{22–24} These anionic functional groups attract cations, such as Li⁺ ions present in the electrolyte, thus increasing their population near the negative electrode. This can lead to an overscreening effect where a layer of cations with greater charge than the negative electrode surface requires a subsequent layer of anions to charge-balance the inner Helmholtz layer.⁷⁶ The overscreening effect gradually decreases with increasing electrode potential.^{26,76} Hence, during charging, the positive electrode stored electrical energy by anion adsorption re-

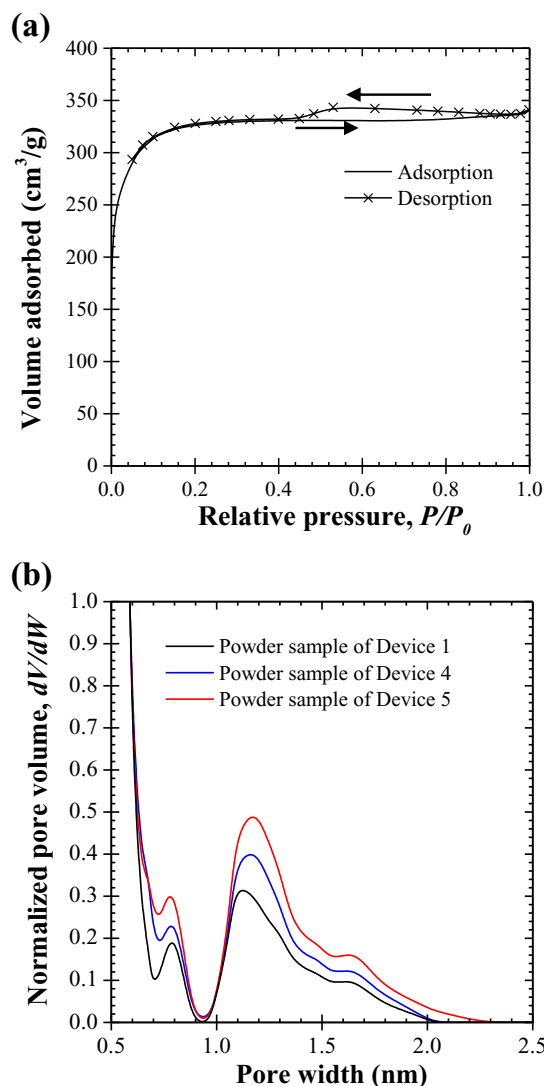


Figure 8. (a) Adsorption/desorption isotherms obtained from nitrogen adsorption for the powder of electrodes materials of Devices 1, 4, and 5. (b) Normalized pore volume derivative versus pore width for the powder of electrodes materials of Devices 1, 4, and 5.

leasing heat to the surroundings. However, the negative electrodes containing CMC (Devices 1, 2, 3, and 5) first charged by anion desorption (i.e., repelling the subsequent layer of anions formed due to overscreening effect) at low potential ($\lesssim 0.5$ V) and then by cation adsorption at higher potential ($\gtrsim 0.5$ V), as observed previously.⁷⁷ This charging sequence, in turn, resulted in endothermic heating at the beginning of the charging step (low potential) and exothermic heating for the rest of the charging step (high potential). Figure 9 illustrates the overscreening effect near the surface of the negative electrode.

Moreover, in Device 3 (w/o TX100), the endothermic heating dominated during the charging step. This can be attributed to competing screening effects between CMC and TX100. The TX100 surfactant selectively attached to the hydrophobic surface of carbons during mixing of the water-based slurries.^{78,79} This resulted in a carbon/TX100/CMC interface in the electrodes that reduces the effective overscreening induced by CMC. Removing TX100 enhanced the overscreening effect as CMC was closer to the activated carbon surface.

Finally, the thermal behavior observed in Devices 1, 2, 3, and 5 with LiPF₆ in EC:DMC was also previously observed for devices using the same electrode composition as Device 1 but with different electrolyte namely 1 M citric acid in DI water and 1 M of tetrabutylammonium

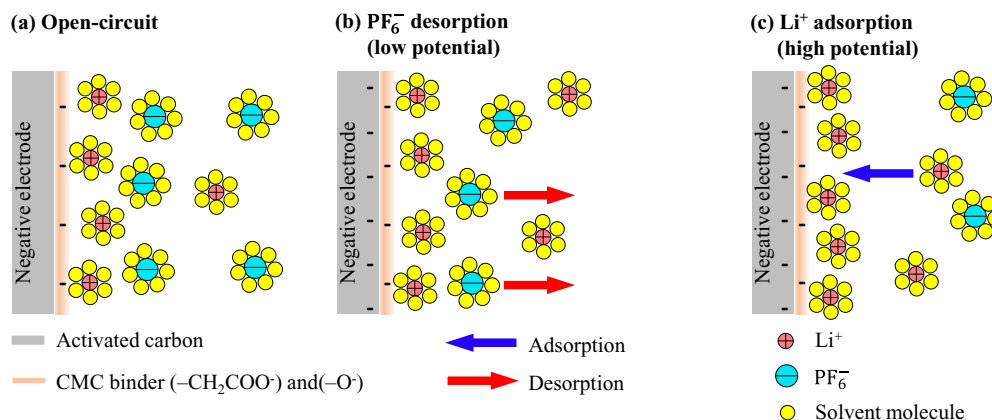


Figure 9. Diagram illustrating the overscreening effect at the negative electrode. (a) In open-circuit, negatively charged CMC groups attract Li^+ cations while PF_6^- anions balance the unsaturated inner Helmholtz layer. (b) At the beginning of the charging step, PF_6^- anions are repelled and desorb from the negative electrode surface. (c) At higher potentials, additional Li^+ cations adsorb to the negative electrode and begin to saturate the inner Helmholtz layer forming the electric double layer.

tetrafluoroborate (TBATFB) in acetonitrile²¹ where the same asymmetry in charging mechanism can also explain the observed thermal behavior.

Conclusions

This study assessed the effect of the electrode composition on heat generation in EDLC devices consisting of two identical carbon-based electrodes. The electrolyte LiPF_6 in EC:DMC was used in all devices. The heat generation rate in each electrode of five EDLC devices with different electrode compositions was measured using a previously described isothermal calorimeter.²¹ First, although removing SBR binder or TX100 surfactant from the electrode composition reduced the internal resistance, it also reduced the capacitance of the device. On the other hand, removing CMC resulted in significant increase in the internal resistance and decrease in the gravimetric capacitance. Second, for all electrode compositions, the irreversible heat generation rate was in excellent agreement with Joule heating predicted from the measured internal resistance and imposed current. Third, in all devices, the reversible heat generation rate in the positive electrode was exothermic during charging and endothermic during discharging. It was also significantly larger than that in the negative electrode of the devices containing CMC binder. Indeed, in the negative electrode containing CMC, the reversible heat generation rate featured both exothermic and endothermic processes during both charging and discharging.²¹ However, in absence of CMC from the electrode, the reversible heat generation rates at the positive and negative electrodes were nearly identical. The asymmetric heating in presence of CMC was attributed to the fact that anionic functional groups formed in the electrodes and interacted with cations in the negative electrode. The latter was charged first by anion desorption (endothermic) followed by cation adsorption (exothermic) as the electrode potential increased. Such asymmetry in charging mechanisms between the positive and negative electrodes explained the observed asymmetry in heat generation. The findings of this study will help to improve our existing thermal model¹⁵ to account for heat generation associated with overscreening effect and asymmetric charging mechanism. Also, the heat generation measurements can be coupled with other experimental techniques, such as nuclear magnetic resonance spectroscopy, X-ray transmission, electrochemical quartz crystal microbalance, and infrared spectroscopy, to quantify the charging mechanism parameter from heat generation in each electrode. Finally, the isothermal calorimeter developed in this study can be used for hybrid pseudocapacitors to provide insight into the heat generation associated with redox reactions and other physicochemical phenomena taking place at the pseudocapacitive electrodes.

Acknowledgment

O.M. is grateful for the financial support provided by King Fahd University of Petroleum and Minerals (KFUPM), Dhahran, Saudi Arabia. J.L., D.A., and B.D. were supported by the Office of Naval Research (under grant N00014-16-1-2164).

List of Symbols

A	Footprint area of the heat flux sensor, cm^2
C_g	Integral gravimetric capacitance, F/g
I	Current, mA
m	Mass of active material loaded into the entire cell, g
n	Cycle number, -
\dot{Q}	Heat generation rate, mW
\bar{Q}	Time-averaged heat generation rate, mW
R_i	Internal resistance for entire EDLC device, Ω
S	Heat flux sensor sensitivity, $\mu\text{V}/(\text{mW}/\text{cm}^2)$
t	Time, s
t_c^-	Time immediately after the beginning of the discharging step, s
t_c^+	Time at the end of the charging step, s
ΔV	Voltage difference generated in the heat flux sensor, μV

Greek

v	Scan rate, mV/s
ψ_s	Potential across an EDLC cell, V

Superscripts and Subscripts

c	Refers to charging step
cd	Refers to charging-discharging cycle
irr, i	Refers to irreversible in electrode "i"
J	Refers to Joule heating
max	Refers to maximum
min	Refers to minimum
T	Refers to entire cell
rev, i	Refers to reversible in electrode "i"
+ or -	Refers to positive or negative electrode

ORCID

Laurent Pilon <https://orcid.org/0000-0001-9459-8207>

References

- L. Zhang, Z. Wang, X. Hu, F. Sun, and D. G. Dorrell, "A comparative study of equivalent circuit models of ultracapacitors for electric vehicles", *Journal of Power Sources*, **274**, 899 (2015).
- S. Koochi-Kamali, V. V. Tyagi, N. A. Rahim, N. L. Panwar, and H. Mokhlis, "Emergence of energy storage technologies as the solution for reliable operation of smart power systems: A review", *Renewable and Sustainable Energy Reviews*, **25**, 135 (2013).
- L. Zhang, X. Hu, Z. Wang, F. Sun, and D. G. Dorrell, "A review of supercapacitor modeling, estimation, and applications: A control/management perspective", *Renewable and Sustainable Energy Reviews*, **81**, 1868 (2018).
- B. Conway, *Electrochemical Supercapacitors: Scientific Fundamentals and Technological Applications*, Kluwer Academic/Plenum, New York, NY, 1999.
- A. Burke, "Ultracapacitors: why, how, and where is the technology", *Journal of Power Sources*, **91**(1), 37 (2000).
- J. Goodenough, H. Abruna, and M. Buchanan, *Basic Research Needs for Electrical Energy Storage: Report of the Basic Energy Sciences Workshop for Electrical Energy Storage*, Office of Basic Energy Sciences, DOESC, April 2-4 2007. <http://www.osti.gov/accomplishments/documents/fullText/ACC0330.pdf>.
- J. Schiffer, D. Linzen, and D. Sauer, "Heat generation in double layer capacitors", *Journal of Power Sources*, **160**(1), 765 (2006).
- J. Miller, "Electrochemical capacitor thermal management issues at high-rate cycling", *Electrochimica Acta*, **52**(4), 1703 (2006).
- M. Sakka, H. Gualous, J. Mierlo, and H. Culcu, "Thermal modeling and heat management of supercapacitor modules for vehicle applications", *Journal of Power Sources*, **194**(2), 581 (2009).
- O. Bohlen, J. Kowal, and D. Sauer, "Ageing behavior of electrochemical double layer capacitors: Part II. Lifetime simulation model for dynamic applications", *Journal of Power Sources*, **173**(1), 626 (2007).
- P. Guillemet, Y. Scudeller, and T. Brousse, "Multi-level reduced-order thermal modeling of electrochemical capacitors", *Journal of Power Sources*, **157**(1), 630 (2006).
- C. Masarapu, H. Zeng, K. Hung, and B. Wei, "Effect of temperature on the capacitance of carbon nanotube supercapacitors", *ACS Nano*, **3**(8), 2199 (2009).
- H. Gualous, H. Louahlia, and R. Gallay, "Supercapacitor characterization and thermal modeling with reversible and irreversible heat effect", *IEEE Transactions on Power Electronics*, **26**(11), 3402 (2011).
- Y. Dandeville, P. Guillemet, O. Crosnier, L. Athouel, and T. Brousse, "Measuring time-dependent heat profiles of aqueous electrochemical capacitors under cycling", *Thermochemica Acta*, **526**(1-2), 1 (2011).
- A. L. D'Entremont and L. Pilon, "First-principles thermal modeling of electric double layer capacitors under constant-current cycling", *Journal of Power Sources*, **246**, 887 (2014).
- A. L. D'Entremont and L. Pilon, "Thermal effects of asymmetric electrolytes in electric double layer capacitors", *Journal of Power Sources*, **273**, 196 (2015).
- X. Zhang, W. Wang, J. Lu, L. Hua, and J. Heng, "Reversible heat of electric double-layer capacitors during galvanostatic charging and discharging cycles", *Thermochemica Acta*, **636**, 1 (2016).
- H. Gualous, H. Louahlia-Gualous, R. Gallay, and A. Miraoui, "Supercapacitor thermal modeling and characterization in transient state for industrial applications", *IEEE Transactions on Industry Applications*, **45**(3), 1035 (2009).
- C. Pasco, Y. Dandeville, Y. Scudeller, P. Guillemet, and T. Brousse, "Calorimetric measurement of the heat generated by a double-layer capacitor cell under cycling", *Thermochemica Acta*, **510**(12), 53 (2010).
- J. Lee, J. Yi, D. Kim, C. Shin, K. Min, J. Choi, and H. Lee, "Modeling of the electrical and thermal behaviors of an ultracapacitor", *Energies*, **7**(12), 8264 (2014).
- O. Munteshari, J. Lau, A. Krishnan, B. Dunn, and L. Pilon, "Isothermal calorimeter for measurements of time-dependent heat generation rate in individual supercapacitor electrodes", *Journal of Power Sources*, **374**, 257 (2018).
- J. Drogenik, M. Gaberscek, R. Dominko, F. Poulsen, M. Mogensen, S. Pejovnik, and J. Jamnik, "Cellulose as a binding material in graphitic anodes for Li ion batteries: a performance and degradation study", *Electrochimica Acta*, **48**(7), 883 (2003).
- L. Qiu, Z. Shao, M. Yang, W. Wang, F. Wang, J. Wan, J. Wang, and H. Duan, "Study on effects of carboxymethyl cellulose lithium (CMC-Li) synthesis and electrospinning on high-rate lithium ion batteries", *Cellulose*, **21**(1), 615 (2014).
- L. Qiu, Z. Shao, D. Wang, F. Wang, W. Wang, and J. Wang, "Novel polymer Li-ion binder carboxymethyl cellulose derivative enhanced electrochemical performance for Li-ion batteries", *Carbohydrate Polymers*, **112**, 532 (2014).
- M. Takeuchi, N. Matubayashi, Y. Kameda, B. Minofar, S. Ishiguro, and Y. Umabayashi, "Free-energy and structural analysis of ion solvation and contact ion-pair formation of Li⁺ with BF₄⁻ and PF₆⁻ in water and carbonate solvents", *Journal of Physical Chemistry B*, **116**(22), 6476 (2012).
- A. Forse, C. Merlet, J. Griffin, and C. Grey, "New perspectives on the charging mechanisms of supercapacitors", *Journal of the American Chemical Society*, **138**(18), 5731 (2016).
- T. Osaka, X. Liu, M. Nojima, and T. Momma, "An electrochemical double layer capacitor using an activated carbon electrode with gel electrolyte binder", *Journal of the Electrochemical Society*, **146**(5), 1724 (1999).
- J. Gamby, P. Taberna, P. Simon, and M. Chesneau, "Studies and characterizations of various activated carbons used for carbon/carbon supercapacitor", *Journal of Power Sources*, **101**(1), 109 (2001).
- V. Khomenko, E. Raymundo-Piñero, and F. Béguin, "Optimisation of an asymmetric manganese oxide/activated carbon capacitor working at 2 V in aqueous medium", *Journal of Power Sources*, **153**(1), 183 (2006).
- Q. Qu, B. Wang, L. Yang, Y. Shi, S. Tian, and Y. Wu, "Study on electrochemical performance of activated carbon in aqueous Li₂SO₄, Na₂SO₄ and K₂SO₄ electrolytes", *Electrochemistry Communications*, **10**(10), 1652 (2008).
- M. Bichat, E. Raymundo-Piñero, and F. Béguin, "High voltage supercapacitor built with seaweed carbons in neutral aqueous electrolyte", *Carbon*, **48**(15), 4351 (2010).
- L. Demarconnay, E. Raymundo-Piñero, and F. Béguin, "A symmetric carbon/carbon supercapacitor operating at 1.6 V by using a neutral aqueous solution", *Electrochemistry Communications*, **12**(10), 1275 (2010).
- B. Wei, J. Tokash, G. Chen, M. Hickner, and B. Logan, "Development and evaluation of carbon and binder loading in low-cost activated carbon cathodes for air-cathode microbial fuel cells", *RSC Advances*, **2**(33), 12751 (2012).
- Q. Gao, L. Demarconnay, E. Raymundo-Piñero, and F. Béguin, "Exploring the large voltage range of carbon/carbon supercapacitors in aqueous lithium sulfate electrolyte", *Energy & Environmental Science*, **5**(11), 9611 (2012).
- W. Gu and G. Yushin, "Review of nanostructured carbon materials for electrochemical capacitor applications: Advantages and limitations of activated carbon, carbide-derived carbon, zeolite-templated carbon, carbon aerogels, carbon nanotubes, onion-like carbon, and graphene", *Wiley Interdisciplinary Reviews: Energy and Environment*, **3**(5), 424 (2014).
- E. Frackowiak and F. Béguin, "Carbon materials for the electrochemical storage of energy in capacitors", *Carbon*, **39**(6), 937 (2001).
- P. Simon and Y. Gogotsi, "Materials for electrochemical capacitors", *Nature Materials*, **7**(11), 845 (2008).
- A. Pandolfo and A. Hollenkamp, "Carbon properties and their role in supercapacitors", *Journal of Power Sources*, **157**(1), 11 (2006).
- E. Frackowiak, "Carbon materials for supercapacitor application", *Physical Chemistry Chemical Physics*, **9**(15), 1774 (2007).
- N. Böckenfeld, S. S. Jeong, M. Winter, S. Passerini, and A. Balducci, "Natural, cheap and environmentally friendly binder for supercapacitors", *Journal of Power Sources*, **221**, 14 (2013).
- K. Kim, J. Hur, S. Jung, and A. Kang, "Electrochemical characteristics of activated carbon/PPy electrode combined with P(VdF-co-HFP)/PVP for EDLC", *Electrochimica Acta*, **50**(2-3), 863 (2004).
- J. Balach, M. Bruno, N. Cotella, D. Acevedo, and C. Barbero, "Electrostatic self-assembly of hierarchical porous carbon microparticles", *Journal of Power Sources*, **199**, 386 (2012).
- H. Buqa, M. Holzappel, F. Krumeich, C. Veit, and P. Novák, "Study of styrene butadiene rubber and sodium methyl cellulose as binder for negative electrodes in lithium-ion batteries", *Journal of Power Sources*, **161**(1), 617 (2006).
- N. Hochgatterer, M. Schweiger, S. Koller, P. Raimann, T. Wöhrle, C. Wurm, and M. Winter, "Silicon/graphite composite electrodes for high-capacity anodes: Influence of binder chemistry on cycling stability", *Electrochimica et Solid-State Letters*, **11**(5), A76 (2008).
- N. Ding, J. Xu, Y. Yao, G. Wegner, I. Lieberwirth, and C. Chen, "Improvement of cyclability of Si as anode for Li-ion batteries", *Journal of Power Sources*, **192**(2), 644 (2009).
- S. Lux, F. Schappacher, A. Balducci, S. Passerini, and M. Winter, "Low cost, environmentally benign binders for lithium-ion batteries", *Journal of The Electrochemical Society*, **157**(3), A320 (2010).
- S. Chou, X. Gao, J. Wang, D. Wexler, Z. Wang, L. Chen, and H. Liu, "Tin/polypyrrole composite anode using sodium carboxymethyl cellulose binder for lithium-ion batteries", *Dalton Transactions*, **40**(48), 12801 (2011).
- F. Courtel, S. Niketic, D. Duguay, Y. Abu-Lebdeh, and I. Davidson, "Water-soluble binders for MCMC carbon anodes for lithium-ion batteries", *Journal of Power Sources*, **196**(4), 2128 (2011).
- M. Mancini, F. Nobili, R. Tossici, M. Wohlfahrt-Mehrens, and R. Marassi, "High performance, environmentally friendly and low cost anodes for lithium-ion battery based on TiO₂ anatase and water soluble binder carboxymethyl cellulose", *Journal of Power Sources*, **196**(22), 9665 (2011).
- W. Zaidi, Y. Oumellal, J. Bonnet, J. Zhang, F. Cuevas, M. Lacroche, J. L. Bobet, and L. Aymard, "Carboxymethylcellulose and carboxymethylcellulose-formate as binders in MgH₂-carbon composites negative electrode for lithium-ion batteries", *Journal of Power Sources*, **196**(5), 2854 (2011).
- A. Krause, P. Kossyrev, M. Oljaca, S. Passerini, M. Winter, and A. Balducci, "Electrochemical double layer capacitor and lithium-ion capacitor based on carbon black", *Journal of Power Sources*, **196**(20), 8836 (2011).
- V. Sivasankaran, C. Marino, M. Chamas, P. Soudan, D. Guyomard, J. Jumas, P. Lippens, L. Monconduit, and B. Lestriez, "Improvement of intermetallic electrochemical behavior by playing with the composite electrode formulation", *Journal of Materials Chemistry*, **21**(13), 5076 (2011).
- J. Bridel, T. Azaïs, M. Morcrette, J. Tarascon, and D. Larcher, "In situ observation and long-term reactivity of Si/CMC composites electrodes for Li-ion batteries", *Journal of The Electrochemical Society*, **158**(6), A750 (2011).
- A. Brandt, P. Isken, A. Lex-Balducci, and A. Balducci, "Adiponitrile-based electrochemical double layer capacitor", *Journal of Power Sources*, **204**, 213 (2012).
- L. Jabbour, R. Bongiovanni, D. Chaussy, C. Gerbaldi, and D. Beneventi, "Cellulose-based Li-ion batteries: a review", *Cellulose*, **20**(4), 1523 (2013).
- M. Casalegno, F. Castiglione, M. Passarello, A. Mele, S. Passerini, and G. Raos, "Association and diffusion of Li⁺ in carboxymethylcellulose solutions for environmentally friendly Li-ion batteries", *ChemSusChem*, **9**(14), 1804 (2016).
- W. Tsai, P. Taberna, and P. Simon, "Electrochemical quartz crystal microbalance (EQCM) study of ion dynamics in nanoporous carbons", *Journal of the American Chemical Society*, **136**(24), 8722 (2014).

58. M. Deschamps, E. Gilbert, P. Azais, E. Raymundo-Piñero, M. Ammar, P. Simon, D. Massiot, and F. Béguin, "Exploring electrolyte organization in supercapacitor electrodes with solid-state NMR", *Nature Materials*, **12**(4), 351 (2013).
59. C. Prehal, D. Weingarh, E. Perre, R. Lechner, H. Amenitsch, O. Paris, and V. Presser, "Tracking the structural arrangement of ions in carbon supercapacitor nanopores using in situ small-angle X-ray scattering", *Energy & Environmental Science*, **8**(6), 1725 (2015).
60. F. Richey, C. Tran, V. Kalra, and Y. Elabd, "Ionic liquid dynamics in nanoporous carbon nanofibers in supercapacitors measured with in operando infrared spectro-electrochemistry", *Journal of Physical Chemistry C*, **118**(38), 21846 (2014).
61. C. Merlet, C. Péan, B. Rotenberg, P. A. Madden, B. Daffos, P. Taberna, P. Simon, and M. Salanne, "Highly confined ions store charge more efficiently in supercapacitors", *Nature Communications*, **4**, 1 (2013).
62. Kuraray Chemical Co. LTD, *High surface area activated carbon technical information*, <http://www.kuraraychemical.com/products/sc/SCcarbon.htm>, accessed March 2018.
63. V. Augustyn, J. Come, M. Lowe, J. Kim, P.-L. Taberna, S. H. Tolbert, H. D. Abruña, P. Simon, and B. Dunn, "High-rate electrochemical energy storage through Li⁺ intercalation pseudocapacitance", *Nature Materials*, **12**(6), 518 (2013).
64. J. Yan, T. Wei, B. Shao, Z. Fan, W. Qian, M. Zhang, and F. Wei, "Preparation of a graphene nanosheet/polyaniline composite with high specific capacitance", *Carbon*, **48**(2), 487 (2010).
65. A. Burke and M. Miller, "Testing of electrochemical capacitors: Capacitance, resistance, energy density, and power capability", *Electrochimica Acta*, **55**(25), 7538 (2010).
66. S. Zhao, F. Wu, L. Yang, L. Gao, and A. Burke, "A measurement method for determination of dc internal resistance of batteries and supercapacitors", *Electrochemistry Communications*, **12**(2), 242 (2010).
67. M. Stoller and R. Ruoff, "Best practice methods for determining an electrode material's performance for ultracapacitors", *Energy & Environmental Science*, **3**(9), 1294 (2010).
68. B.-A. Mei, O. Munteshari, J. Lau, B. Dunn, and L. Pilon, "Physical interpretations of Nyquist plots for EDLC electrodes and devices", *Journal of Physical Chemistry C*, **122**(1), 194 (2018).
69. C. O. Ania, J. Pernak, F. Stefaniak, E. Raymundo-Piñero, and F. Béguin, "Polarization-induced distortion of ions in the pores of carbon electrodes for electrochemical capacitors", *Carbon*, **47**(14), 3158 (2009).
70. S. H. Lapidus, N. N. Rajput, X. Qu, K. W. Chapman, K. A. Persson, and P. J. Chupas, "Solvation structure and energetics of electrolytes for multivalent energy storage", *Phys. Chem. Chem. Phys.*, **16**(40), 21941 (2014).
71. J. Rouquerol, D. Avnir, C. Fairbridge, D. Everett, J. Haynes, N. Pernicone, J. Ramsay, K. Sing, and K. Unger, "Recommendations for the characterization of porous solids (Technical Report)", *Pure and Applied Chemistry*, **66**(8), 1739 (1994).
72. J. Moreno-Piraján, J. Tirano, B. Salamanca, and L. Giraldo, "Activated carbon modified with copper for adsorption of propanethiol", *International Journal of Molecular Sciences*, **11**(3), 927 (2010).
73. D. Nan, Z. Huang, R. Lv, L. Yang, J. Wang, W. Shen, Y. Lin, X. Yu, L. Ye, H. Sun, and F. Kang, "Nitrogen-enriched electrospun porous carbon nanofiber networks as high-performance freestanding electrode materials", *Journal of Materials Chemistry A*, **2**(46), 19678 (2014).
74. A. Forse, J. Griffin, C. Merlet, J. Carretero-Gonzalez, A. Raji, N. Trease, and C. Grey, "Direct observation of ion dynamics in supercapacitor electrodes using in situ diffusion NMR spectroscopy", *Nature Energy*, **2**(3), 16216 (2017).
75. A. L. D'Entremont and L. Pilon, "First-principles thermal modeling of hybrid pseudo-capacitors under galvanostatic cycling", *Journal of Power Sources*, **335**, 172 (2016).
76. M. Bazant, B. Storey, and A. Kornyshev, "Double layer in ionic liquids: Overscreening versus crowding", *Physical Review Letters*, **106**(4), 46102 (2011).
77. M. Levi, N. Levy, S. Sigalov, G. Salitra, D. Aurbach, and J. Maier, "Electrochemical quartz crystal microbalance (EQCM) studies of ions and solvents insertion into highly porous activated carbons", *Journal of the American Chemical Society*, **132**(38), 13220 (2010).
78. B. Lestriez, S. Bahri, I. Sandu, L. Roué, and D. Guyomard, "On the binding mechanism of CMC in Si negative electrodes for Li-ion batteries", *Electrochemistry Communications*, **9**(12), 2801 (2007).
79. W. Porcher, B. Lestriez, S. Jouanneau, and D. Guyomard, "Optimizing the surfactant for the aqueous processing of LiFePO₄ composite electrodes", *Journal of Power Sources*, **195**(9), 2835 (2010).